

# Semi-empirical model of the effect of scattering on single fiber fluorescence intensity measured on a turbid medium

S.C. Kanick,\* D. J. Robinson, H. J. C. M. Sterenborg, and A. Amelink

Center for Optical Diagnostics and Therapy, Department of Radiation Oncology, Erasmus Medical Center, PO Box 2040, 3000 CA Rotterdam, The Netherlands

\*s.kanick@erasmusmc.nl

**Abstract:** Quantitative determination of fluorophore content from fluorescence measurements in turbid media, such as tissue, is complicated by the influence of scattering properties on the collected signal. This study utilizes a Monte Carlo model to characterize the relationship between the fluorescence intensity collected by a single fiber optic probe ( $F_{SF}$ ) and the scattering properties. Simulations investigate a wide range of biologically relevant scattering properties specified independently at excitation ( $\lambda_x$ ) and emission ( $\lambda_m$ ) wavelengths, including reduced scattering coefficients in the range  $\mu'_s(\lambda_x) \in [0.1 - 8] \text{mm}^{-1}$  and  $\mu'_s(\lambda_m) \in [0.25 - 1] \times \mu'_s(\lambda_x)$ . Investigated scattering phase functions ( $P(\theta)$ ) include both Henyey-Greenstein and Modified Henyey-Greenstein forms, and a wide range of fiber diameters ( $d_f \in [0.2 - 1.0] \text{mm}$ ) was simulated. A semi-empirical model is developed to estimate the collected  $F_{SF}$  as the product of an effective sampling volume, and the effective excitation fluence and the effective escape probability within the effective sampling volume. The model accurately estimates  $F_{SF}$  intensities ( $r=0.999$ ) over the investigated range of  $\mu'_s(\lambda_x)$  and  $\mu'_s(\lambda_m)$ , is insensitive to the form of the  $P(\theta)$ , and provides novel insight into a dimensionless relationship linking  $F_{SF}$  measured by different  $d_f$ .

© 2011 Optical Society of America

**OCIS codes:** (060.2310) Fiber optics; (290.7050) Turbid Media; (170.3660) Light propagation in tissues; (300.6280) Spectroscopy, fluorescence and luminescence.

## References and links

1. N. Thekkek, S. Anandasabapathy, and R. Richards-Kortum, "Optical molecular imaging for detection of Barrett's-associated neoplasia," *World J. Gastroenterol.* **17**:53-62 (2011).
2. V. Ntziachristos, "Going deeper than microscopy: the optical imaging frontier in biology," *Nat. Methods.* **7**:603-614 (2010).
3. S.L. Gibbs-Strauss, J.A. O'Hara, S. Srinivasan, P. J. Hoopes, T. Hasan, and B. W. Pogue, "Diagnostic detection of diffuse glioma tumors in vivo with molecular fluorescent probe-based transmission spectroscopy," *Med. Phys.* **36**:974-983 (2009).
4. C. C. Lee, B. W. Pogue, R. R. Strawbridge, K. L. Moodie, L. R. Bartholomew, G. C. Burke, and P. J. Hoopes, "Comparison of photosensitizer (AIPcS2) quantification techniques: in situ fluorescence microsampling versus tissue chemical extraction," *Photochem. Photobiol.* **74**:453-460 (2001).
5. J. C. Finlay, T. C. Zhu, A. Dimofte, D. Stripp, S. B. Malkowicz, T. M. Busch, and S. M. Hahn, "Interstitial fluorescence spectroscopy in the human prostate during motexafin lutetium-mediated photodynamic therapy," *Photochem. Photobiol.* **82**:1270-1278 (2006).
6. D. J. Robinson, M. B. Karakulluku, B. Kruijt, S. C. Kanick, R. L. P. van Veen, A. Amelink, H. J. C. M. Sterenborg, M. J. H. Witjes, and I. B. Tan, "Optical spectroscopy to guide photodynamic therapy of head and neck tumors," *IEEE J. Sel. Top. Quantum Electron.* **16**:854-862 (2010).

7. A. J. Welch, C. Gardner, R. Richards-Kortum, E. Chan, G. Criswell, J. Pfefer, and S. Warren, "Propagation of fluorescent light," *Lasers Surg. Med.* **21**:166-178 (1997).
8. J. Wu, M. S. Feld, and R. P Rava, "Analytical model for extracting intrinsic fluorescence in turbid media," *Appl. Opt.* **19**:3585-3595 (1993).
9. C. M. Gardner, S. L. Jacques, and A. J. Welch, "Fluorescence spectroscopy of tissue: recovery of intrinsic fluorescence from measured fluorescence," *Appl. Opt.* **35**:1780-1792 (1996).
10. M. G. Müller, I. Georgakoudi, Q. Zhang, J. Wu, and M. S. Feld, "Intrinsic fluorescence spectroscopy in turbid media: disentangling effects of scattering and absorption," *Appl. Opt.* **40**:4633-4646 (2001).
11. Q. Zhang, M. G. Müller, J. Wu, and M. S. Feld, "Turbidity-free fluorescence spectroscopy of biological tissue," *Opt. Lett.* **25**:1451-1453 (2000).
12. J. C. Finlay and T. H. Foster, "Recovery of hemoglobin oxygen saturation and intrinsic fluorescence with a forward-adjoint model," *Appl. Opt.* **44**:1917-1933 (2005).
13. G. M. Palmer and N. Ramanujam, "Monte-carlo-based model for the extraction of intrinsic fluorescence from turbid media," *J. Biomed. Opt.* **13**:024017 (2008).
14. G. M. Palmer, R. J. Viola, T. Schroeder, P. S. Yarmolenko, M. W. Dewhirst, and N. Ramanujam, "Quantitative diffuse reflectance and fluorescence spectroscopy: tool to monitor tumor physiology in vivo," *J. Biomed. Opt.* **14**:024010 (2009).
15. R. H. Wilson, M. Chandra, J. Scheiman, D. Simeone, B. McKenna, J. Purdy, and M. A. Mycek, "Optical spectroscopy detects histological hallmarks of pancreatic cancer," *Opt. Express* **17**:17502-17516 (2009).
16. A. Kim, M. Khurana, Y. Moriyama, and B. C. Wilson, "Quantification of in vivo fluorescence decoupled from the effects of tissue optical properties using fiber-optic spectroscopy measurements," *J. Biomed. Opt.* **15**:067006 (2010).
17. B. W. Pogue and G. Burke, "Fiber-optic bundle design for quantitative fluorescence measurement from tissue," *Appl. Opt.* **37**: 7429-7436 (1998).
18. T. J. Pfefer, K. T. Schomacker, M. N. Ediger, and N. S. Nishioka, "Light propagation in tissue during fluorescence spectroscopy with single-fiber probes," *IEEE J. Sel. Top. Quantum Electron.* **7**:1004-1012 (2001).
19. K. R. Diamond, M. S. Patterson, and T. J. Farrell, "Quantification of fluorophore concentration in tissue-simulating media by fluorescence measurements with a single optical fiber," *Appl. Opt.* **42**:2436-2442 (2003).
20. H. Stepp, T. Beck, W. Beyer, C. Pfaller, M. Schuppler, R. Sroka, and R. Baumgartner, "Measurement of fluorophore concentration in turbid media by a single optical fiber," *Medical Laser Application* **22**:23-34 (2007).
21. A. Amelink, B. Kruijt, D. J. Robinson, and H. J. C. M. Sterenborg, "Quantitative fluorescence spectroscopy in turbid media using fluorescence differential path length spectroscopy," *J. Biomed. Opt.* **13**:054051 (2008).
22. M. Sinaasappel and H. J. C. M. Sterenborg, "Quantification of the hematoporphyrin derivative by fluorescence measurement using dual-wavelength excitation and dual-wavelength detection," *Appl. Opt.* **32**:541-548 (1993).
23. R. Weersink, M. S. Patterson, K. Diamond, S. Silver, and N. Padgett, "Noninvasive measurement of fluorophore concentration in turbid media with a simple fluorescence /reflectance ratio technique," *Appl. Opt.* **40**:6389-6395 (2001).
24. S. C. Kanick, U. A. Gamm, M. Schouten, H. J. C. M. Sterenborg, D. J. Robinson, and A. Amelink, "Measurement of the reduced scattering coefficient of turbid media using single fiber reflectance spectroscopy: fiber diameter and phase function dependence," *Biomed. Opt. Express* **2**:1687-1702 (2011).
25. S. C. Kanick, U. A. Gamm, H. J. C. M. Sterenborg, D. J. Robinson, and A. Amelink, "Method to quantitatively estimate wavelength-dependent scattering properties from multi-diameter single fiber reflectance spectra measured in a turbid medium," *Opt. Lett.* **36**:2997-2999 (2011).
26. U. A. Gamm, S. C. Kanick, H. J. C. M. Sterenborg, D. J. Robinson, and A. Amelink, "Measurement of tissue scattering properties using multi-diameter single fiber reflectance spectroscopy: *in silico* sensitivity analysis," *Biomed. Opt. Express* **2**:3150-3166 (2011).
27. L. Wang, S. Jacques, and L. Zheng, "MCML—Monte Carlo modeling of light transport in multi-layered tissues," *Comp. Meth. Prog. Biomed.* **47**:131-146 (1995).
28. W. Cheong, S. A. Prahl, and A. J. Welch, "A review of the optical properties of biological tissues," *IEEE J. Quant. Electron.* **26**:2166-2185 (1990).
29. A. Amelink, D. J. Robinson, and H. J. C. M. Sterenborg, "Confidence intervals on fit parameters derived from optical reflectance spectroscopy measurements," *J. Biomed. Opt.* **13**:05040144 (2008).
30. E. J. Hudson, M. R. Stringer, F. Cairnduff, D. V. Ash, and M. A. Smith, "The optical properties of skin tumours measured during superficial photodynamic therapy," *Laser. Med. Sci.* **9**:99-103 (1994).
31. F. Bevilacqua and C. Depeursinge, "Monte Carlo study of diffuse reflectance at source-detector separations close to one transport mean free path," *J. Opt. Soc. Am. A* **16**:2935-2945 (1999).
32. A. Kienle, F. Forster, and R. Hibst, "Influence of the phase function on determination of the optical properties of biological tissue by spatially resolved reflectance," *Opt. Lett.* **26**:1571-1573 (2001).

## 1. Introduction

Detection and quantitation of fluorescence is important for many biomedical and clinical applications. The optical detection of fluorescent endogenous compounds [1] such as collagen and NADH, or exogenous compounds that include labelled markers, can be used for diagnostic purposes [2, 3]. The measurement of therapeutic compounds, such as photosensitizers used in photodynamic therapy [4, 5], may provide insight into the pharmacokinetic distribution and pharmacodynamic activity in tissues of interest and may play a role in monitoring administered therapies [6]. However, quantitation of fluorescence in tissue *in vivo* is complicated by the influence of the tissue optical properties on the collected fluorescence signal [7]. Absorption by chromophores within the tissue causes attenuation that is (non-linearly) proportional to the absorption coefficient at the excitation and emission wavelengths. Scattering within tissue is known to have a complicated effect on fluorescence measurements: the properties at the excitation wavelength ( $\lambda_x$ ) affect the delivered excitation light profile and the properties at the emission wavelength ( $\lambda_m$ ) determine the likelihood that fluorescent emission photons propagate to the detector used in the measurement. In order to quantitatively analyze fluorescence in tissue, it is important to obtain an intrinsic fluorescence signal that is independent of the optical property effects [8–10]. This approach would yield a quantity that is proportional to the product of the concentration and quantum yield of the fluorophore within the optically sampled volume, and would be comparable between measurements of samples with different background tissue optical properties.

Previously developed methods to extract intrinsic fluorescence spectra involve the acquisition of a paired measurement of fluorescence and white-light reflectance, where the latter is used to inform a correction of the influence of optical properties on fluorescence. This general approach has been extensively investigated for multi-fiber fluorescence probes, with separate source(s) and detectors [8–16]. These probes collect multiply scattered, or diffuse, light and sample volumes of tissue on the orders of several mm<sup>3</sup>. An alternative approach for fluorescence measurements is to use small fiber optic probes that utilize a single optical fiber to both deliver excitation light and collect emitted fluorescence [5, 17–21]; such a measurement results in a localized sampling volume, with the majority of the collected signal originating very close to the probe face [18]. Single fiber fluorescence (SFFL) measurements collect photons that have undergone few scattering events, and in turn, have a very small light propagation path, making the collected intensity less sensitive to tissue chromophores and scattering properties than diffuse measurements. The influence of scattering on collected SFFL intensity has been previously investigated and was observed to be nonlinear and fiber-diameter specific [20]. Furthermore, the SFFL intensity was observed to be insensitive to variations in the scattering phase function (PF) [19]. The underlying mechanism of these factors was not fully elucidated. These and other previous studies accounted for the influence of scattering on SFFL by characterizing ranges of fiber diameters and optical property combinations where the SFFL signal was insensitive to optical properties [17, 19, 20]. While this approach may be useful for specific applications with well-known ranges of optical properties, it does not return a quantitative description of tissue fluorescence that is independent of optical properties, and therefore, does not provide a reliable comparison of measurements performed on different tissue locations or with different fiber diameters.

To the best of the authors' knowledge, there is currently no analytical or empirical description of the influence of scattering properties on the fluorescence intensity sampled by a single fiber. The present study investigates the detailed mechanisms associated with the influence of scattering properties on the SFFL intensity measured in a turbid medium, and develops a mathematical model to correct for these influences. This represents a first step towards a full correction of collected SFFL intensities for the influence of optical properties (*i.e.* both scattering

and absorption). Monte Carlo (MC) simulations are used to investigate SFFL measurement of a wide range of scattering properties that are independently specified at excitation and emission wavelengths; simulations also included a wide range of fiber diameters. Simulated data are used to identify and characterize a semi-empirical model that expresses SFFL intensity as a function of a dimensionless scattering property (given as the product of scattering coefficient and fiber diameter). The resulting model is applicable to all investigated fiber diameters and provides insight into the physics underlying the SFFL measurement.

## 2. Methods

### 2.1. Monte Carlo model

The Monte Carlo (MC) code utilized in this study is a customized version of the MCML program [27] that is modified to emulate single fiber fluorescence measurements of a homogeneous turbid medium. The code allows independent specification of both the scattering coefficient ( $\mu_s$ ) and scattering phase function ( $P(\theta)$ ) at excitation ( $\lambda_x$ ) and emission ( $\lambda_m$ ) wavelengths. Excitation photons were initialized by selecting a location on the fiber face, which is modeled in contact with the turbid medium at the air/medium interface  $z = 0$ , and were launched into a direction within the fiber cone of acceptance, where the acceptance angle was given as  $\Theta_a = \text{asin}\left(\frac{NA}{n_{\text{medium}}}\right)$ ; both the location and the direction were sampled from uniform distributions. The index of refraction ( $n$ ) of the medium and fiber were specified at 1.37 and 1.45, respectively, and were held constant between  $\lambda_x$  and  $\lambda_m$ . The numerical aperture (NA) of the fiber was set as 0.22. Reflection and refraction due to the index of refraction mismatch at the medium/fiber and the surrounding medium/air interface were calculated using the Fresnel equations and Snell's law. This code simulated propagation of excitation photons by stochastically selecting step sizes ( $s_n$ ) from an exponential distribution weighted by  $\mu_s(\lambda_x)$ , and each scattering angle was selected from  $P(\theta)(\lambda_x)$ . At discrete points along each individual step, excitation photons were stochastically checked for a fluorescence event, with the probability given by  $e^{-\mu_a^f s_n}$ , where  $\mu_a^f$  is the specific absorption coefficient of the fluorophore. Stochastic absorption by the fluorophore resulted in an isotropic scattering event, and propagation of the emission photon was continued at the scattering properties at  $\lambda_m$ . Emission photons propagating within the turbid medium that cross the medium interfacial boundary at  $z = 0$ , were checked for contact with the fiber face; those in contact and traveling at an angle within the fiber cone of acceptance were collected, the rest were terminated. Excitation photons contacting the fiber face at any angle were terminated and did not contribute to the collected fluorescence intensity. This calculation returned the fraction of the number of collected fluorescence photons and the number of excitation photons for each simulation, calculated as:

$$F_{SF \text{ ratio}}^{MC} = \frac{TMPC}{TXPL} \quad (1)$$

where TXPL is the total number of excitation photons launched and TMPC the total number of emission photons collected. Excitation and emission photons propagating within the medium far from the fiber face do not contribute to the collected fluorescence intensity and were terminated at a hemispherical limit from the fiber face of  $10\frac{d_{fib}}{\mu_s}$ ; a limit that was confirmed to not influence model outputs for the range of optical properties investigated in this study. Model outputs of  $F_{SF \text{ ratio}}^{MC}$  were validated by comparison with previously published fluorescence intensities over a range of background optical properties [18].

During photon propagation, the photon positions were tracked in a discrete voxel grid to yield individual 2D( $r,z$ ) probability density profiles for all incident excitation photons, for all fluorescence emission photons, and a separate profile for all collected fluorescence photons. Specif-

ically, the code generated 2D maps of the relative excitation light fluence ( $\Phi_x(r, z) [m^{-2}]$ ), which is calculated as previously described [27], and of the photon probability density of fluorescence collected by the fiber ( $F_{col}(r, z) [m^{-3}]$ ), which represents the spatial location of origin for all collected fluorescence photons [18]. Note that these quantities involve ratio calculations and do not depend on the number of launched excitation photons. From these maps, the dimensionless escape probability density profile of emission photons ( $H(r, z) = \frac{F_{col}(r, z)}{\mu_a^f(r, z)\Phi_x(r, z)}$ ), which is defined as the probability of emission photon collection per fluorescence photon generated, was calculated. Note that the fluorescence generated at a location  $(r, z)$  is proportional to the product of  $\mu_a^f(r, z)$  and  $\Phi_x(r, z)$ . These 2-D spatial profiles were used to calculate effective values for the volume sampled and the excitation fluence and escape probability within the sampled volume, by properly weighting each respective quantity by the collected fluorescence that originated at the corresponding location. A scalar effective optical sampling depth ( $\langle Z^{MC} \rangle [m]$ ) is calculated as the weighted average depth of the collected emission photons, given as

$$\langle Z^{MC} \rangle = \frac{\sum_{i=1}^{n_z} z_i \left( \sum_{j=1}^{n_r} F_{col}(r_j, z_i) \Delta a_j \right) \Delta z}{\sum_{i=1}^{n_z} \left( \sum_{j=1}^{n_r} F_{col}(r_j, z_i) \Delta a_j \right) \Delta z} \quad (2)$$

where  $\Delta a_j$  is the area of a voxel at position  $r_j$  and  $\Delta z$  is the z-dimensional length of each voxel [27]. A scalar effective excitation fluence within the optically sampled volume ( $\langle \Phi_x^{MC} \rangle [m^{-2}]$ ) was calculated from the weighted average of  $\Phi_x(r, z)$ , with the collected fluorescence photon probability density  $F_{col}(r, z)$  as weight factors, as

$$\langle \Phi_x^{MC} \rangle = \frac{\sum_{i=1}^{n_z} \left( \sum_{j=1}^{n_r} \Phi_x(r_j, z_i) F_{col}(r_j, z_i) \Delta a_j \right) \Delta z}{\sum_{i=1}^{n_z} \left( \sum_{j=1}^{n_r} F_{col}(r_j, z_i) \Delta a_j \right) \Delta z} \quad (3)$$

Similarly, a scalar for the effective escape probability within the optically sampled volume ( $\langle H_m^{MC} \rangle [-]$ ) was calculated from the weighted average of the escape probability density distribution  $H_m(r, z)$ , with the collected fluorescence photon probability density  $F_{col}(r, z)$  as weight factors, as

$$\langle H_m^{MC} \rangle = \frac{\sum_{i=1}^{n_z} \left( \sum_{j=1}^{n_r} H_m(r_j, z_i) F_{col}(r_j, z_i) \Delta a_j \right) \Delta z}{\sum_{i=1}^{n_z} \left( \sum_{j=1}^{n_r} F_{col}(r_j, z_i) \Delta a_j \right) \Delta z} \quad (4)$$

## 2.2. Monte Carlo simulations

MC simulations were performed over a broad range of biologically relevant [28] reduced scattering coefficient ( $\mu_s'$ ) values that were individually specified at  $\lambda_x$  and  $\lambda_m$ , with:  $\mu_s'(\lambda_x) = [0.1, 0.25, 0.5, 1, 2, 4, 8] \text{ mm}^{-1}$  and  $\mu_s'(\lambda_m) = [0.25, 0.5, 0.75, 1.0] \times \mu_s'(\lambda_x)$ . This series of simulations was performed at all specified  $\mu_s'$  combinations using the Modified Henyey-Greenstein (MHG) PF [24] with the anisotropy specified as  $g_1 = 0.9$  and  $\gamma$ , which characterizes the first two moments of the phase function and is given as  $\gamma = \frac{1-g_2}{1-g_1}$ , was set as  $\gamma = 1.4$ .

A subset of simulations further investigated the influence of PF over a selected range of reduced scattering values,  $\mu'_s(\lambda_x) = [0.5, 1, 2] \text{ mm}^{-1}$  and  $\mu'_s(\lambda_m) = [0.5, 1.0] \times \mu'_s(\lambda_x)$ , using the Henyey-Greenstein (HG) PF with  $g_1 = [0.5, 0.9]$  and  $\gamma = [1.5, 1.9]$  and the MHG PF with combinations of  $g_1 = [0.8, 0.9, 0.95]$  and  $\gamma = [1.4, 1.5, 1.6, 1.7, 1.8, 1.9]$ .

Additionally, simulations investigated variations in  $NA$  from the baseline value of 0.22 over the range  $[0.1 - 0.4]$ . This subset of simulations was performed using the same scattering properties as the subset of simulations used to investigate the influence of PF.

Simulations of each possible combination of scattering properties were performed for a range of fiber diameters, with  $d_f = [0.2, 0.4, 0.6, 1.0] \text{ mm}$ . The absorption of the fluorophore was given as  $\mu_a^f = 0.1 \text{ mm}^{-1}$  in all simulations; this study did not consider absorption due to background chromophores. In total, the data presented in this study include 616 MC simulations, each launching at least 20 million photons.

### 2.3. Semi-empirical model of the single fiber fluorescence intensity

The fluorescence signal  $F$  (in units of Joules [J]) collected by a fiber optic probe is given by the integral [12]

$$F = (\lambda_x/\lambda_m) \mu_a^f Q^f \int_V \Phi_x(\mathbf{r}) H_m(\mathbf{r}) d^3r \quad (5)$$

where  $\Phi_x(\mathbf{r})$  [ $\text{J m}^{-2}$ ] is the excitation fluence,  $H_m(\mathbf{r})$  [-] is the escape probability of emission photons,  $\mu_a^f$  [ $\text{m}^{-1}$ ] is the absorption coefficient of the fluorophore at the excitation wavelength, and  $Q^f$  [-] is the fluorescence quantum yield. The ratio  $(\lambda_x/\lambda_m)$  accounts for the difference in photon energy between the emission and excitation wavelengths, and will be omitted in the remainder of the equations since in the Monte Carlo simulations this ratio is set to unity. The volume integral of  $\Phi_x H_m$  is dependent on optical properties; however the intrinsic fluorescence, given by the product of  $\mu_a^f Q^f$  is independent of optical properties and has dimensions [ $\text{m}^{-1}$ ].

This study develops an approximate solution to Eq. (5) for a SFFL measurement by representing the volume integral of  $\Phi_x H_m$  as the product of an effective optically sampled volume and the effective  $\Phi_x$  and  $H_m$  values within that volume, thus redefining Eq. (5) as,

$$F_{SF} \approx \mu_a^f Q^f \langle V \rangle \langle \Phi_x^V \rangle \langle H_m^V \rangle \quad (6)$$

where  $\langle V \rangle$  is the effective sampling volume, and  $\langle \Phi_x^V \rangle$  and  $\langle H_m^V \rangle$  are the effective excitation fluence and effective escape probability within the sampled volume, respectively. These quantities can be related to the scalar outputs from the MC simulations defined in Section 2.1 by approximating the effective sampling volume as

$$\langle V \rangle \approx A_1 \langle Z^{MC} \rangle d_f^2 \quad (7)$$

with  $\langle Z^{MC} \rangle$  the effective sampling depth and  $A_1$  a proportionality factor that depends on the geometrical shape of the effective volume. Furthermore, the effective excitation fluence and escape probability within the sampled volume can be written as

$$\langle \Phi_x^V \rangle = P_x \langle \Phi_x^{MC} \rangle \quad (8)$$

$$\langle H_m^V \rangle = \langle H_m^{MC} \rangle \quad (9)$$

where  $P_x$  is the total power output from the fiber, which in these simulations is proportional to the number of launched photons TXPL. Eq. (8) properly accounts for differences in the incident excitation intensity emitted from the fiber face for different numbers of launched photons

TXPL, but does not correct for differences in incident excitation light intensity due to differences in fiber diameter. Since the incident excitation intensity is inversely proportional to the fiber area, it is expected that  $\Phi_x^{MC}$  scales with  $d_f^{-2}$ . Substituting Eqs. (7-9) in Eq. (6), dividing by  $P_x$ , which is then replaced by TXPL yields SFFL expressed as a percentage of incident excitation photons, as

$$F_{SF\ ratio}^{MC} = \frac{TMPC}{TXPL} \approx A_1 \mu_a^f Q^f \langle Z^{MC} \rangle d_f^2 \langle \Phi_x^{MC} \rangle \langle H_m^{MC} \rangle \quad (10)$$

As described in Section 2.1, the MC simulations used in this study were used to return information about how SFFL intensity and the effective terms presented in Eq. (10) are influenced by scattering properties at the excitation and emission wavelengths. Inspection of the simulated data led to the identification of candidate empirical expressions to describe each quantity; from these a set of equations was selected on the basis of fit quality and model simplicity, and is given as

$$\langle Z^{MC} \rangle = d_f A_2 (\mu'_{s,avg} d_f)^{-A_3} \quad (11)$$

$$\langle \Phi_x^{MC} \rangle = d_f^{-2} B_1 e^{\frac{-1}{B_2 (\mu'_s(\lambda_x) d_f)^{+1}}} \quad (12)$$

$$\langle H_m^{MC} \rangle = C_1 e^{\frac{-C_3}{C_2 (\mu'_s(\lambda_m) d_f)^{+1}}} \quad (13)$$

where  $[A_{1,2,3}, B_{1,2}, C_{1,2,3}]$  in Eqs. (10-13) are fitted parameters. The effective sampling depth  $\langle Z^{MC} \rangle$  was observed to follow an exponential decay with respect to the product of  $\mu'_{s,avg}(\lambda_x, \lambda_m) d_f$ , where  $\mu'_{s,avg}(\lambda_x, \lambda_m)$  is calculated as the average of  $\mu'_s(\lambda_x)$  and  $\mu'_s(\lambda_m)$ . The effective relative excitation fluence  $\langle \Phi_x^{MC} \rangle$  was observed to scale with  $d_f^{-2}$  as expected, and to follow an exponential expression that depended on the product  $\mu'_s(\lambda_x) d_f$ . The effective escape probability  $\langle H_m^{MC} \rangle$  was observed to follow an exponential function that depended on the product  $\mu'_s(\lambda_m) d_f$ . Substituting Eqs. (11-13) into Eq. (10) results in

$$\frac{F_{SF\ ratio}^{MC}}{\mu_a^f Q^f d_f v_n} = \zeta_1 (\mu'_{s,avg} d_f)^{-\zeta_2} e^{\left( \frac{-1}{\zeta_2 (\mu'_s(\lambda_x) d_f)^{+1}} - \frac{\zeta_3}{\zeta_2 (\mu'_s(\lambda_m) d_f)^{+1}} \right)} \quad (14)$$

where  $[\zeta_1, \zeta_2, \zeta_3]$  are fitted parameters. This represents a reduction from the parameter set specified in Eqs. (10-13). Here,  $\zeta_1$  represents the product of  $A_1, A_2, B_1$  and  $C_1$ . Fitted parameters were estimated using a Levenberg-Marquardt algorithm coded into a Matlab script (version 2009a, MathWorks). Confidence intervals of the estimated parameters were calculated from the square root of the diagonal of the covariance matrix [29]. During the model fit analysis, the estimated values for  $A_3, B_2$  and  $C_2$  were observed to have overlapping 95% confidence intervals [29], which led to the reduction of these terms to a single fitted parameter,  $\zeta_2$ . This substitution did not result in a significant increase in model residual error.

Continuing the description of the terms in Eq. (14),  $v_n$  represents the influence of the index of refraction mismatch at  $z = 0$  (between fiber/medium and the annular air/medium interfaces). This parameter was found to be dependent on  $d_f$ , and to follow the form:  $v_n = \frac{1}{1+\varepsilon d_f}$ , with  $\varepsilon = 0.17\text{mm}^{-1}$ . This form was identified from comparing simulations of the fiber surrounded by air with the fiber surrounded by a refractive index matching the fiber; this factor is analogous to offset factors described previously [11].

Equation (14) represents a fiber diameter dependent expression that relates fluorescence collected by a single fiber with diameter  $d_f$  that has been distorted by scattering at excitation and

emission wavelengths, to the intrinsic fluorescence  $\mu_a^f Q^f$  within the sampled turbid medium. For brevity, the quantity  $F_{SF}^{sim}$  [m] will be used throughout this manuscript to refer to the expression

$$F_{SF}^{sim} = \frac{F_{SF}^{MC} \text{ ratio}}{\mu_a^f Q^f v_n} \quad (15)$$

### 3. Results

#### 3.1. Influence of scattering properties and fiber diameter on $F_{SF}^{sim}$

##### 3.1.1. Case I: $\mu_s'(\lambda_x) = \mu_s'(\lambda_m)$

MC simulations investigated the relationship between single fiber fluorescence and variations in  $\mu_s'$ , initially specified as equivalent at  $\lambda_x$  and  $\lambda_m$ , and varied over the range  $[0.1 - 8.0] \text{ mm}^{-1}$ . Figure 1 A and B shows  $F_{SF}^{sim}$  collected by single fiber probes with  $d_f \in [0.2 - 1.0] \text{ mm}$ . These data show a fiber-diameter specific nonlinear relationship between  $F_{SF}^{sim}$  and  $\mu_s'$ . Inspection of  $F_{SF}^{sim}$  data sampled by the  $d_f = 0.2 \text{ mm}$  fiber shows a 60% decrease in intensity as  $\mu_s'$  increases across the investigated range. However, the  $d_f = 1.0 \text{ mm}$  fiber shows an initial decrease in  $F_{SF}^{sim}$  of 25% as  $\mu_s'$  increases from 0.1 to 0.5  $\text{mm}^{-1}$ , and  $F_{SF}^{sim}$  then doubles in intensity as  $\mu_s'$  increases from 0.5 to 8  $\text{mm}^{-1}$ .

Inspection of the fiber-diameter specific  $F_{SF}^{sim}$  vs.  $\mu_s'$  profiles led to the identification of two dimensionless transformations that are important for interpretation of the data. First, transformation of the abscissa to dimensionless reduced scattering, given as the product  $\mu_s' d_f$ , shifted the  $F_{SF}^{sim}$  data on the x-axis such that the minimum  $F_{SF}^{sim}$  values for each fiber specific profile aligned at the  $\mu_s' d_f$  value of 0.5; the effect of this transformation is clearly shown in Figures 1 C and D. Second, expression of the ordinate as the dimensionless ratio of  $F_{SF}^{sim} / d_f$  brought measurements from different fiber diameters onto an overlapping profile; this observed proportionality between fiber diameter and collected fluorescence is consistent with previous analysis of SFFL [20]. Figures 1 E and F show the resulting dimensionless relationship between  $F_{SF}^{sim} / d_f$  and  $\mu_s' d_f$  that is observed for measurements from all investigated fiber diameters; there exists more than a factor of 2 variation in the observed magnitude of  $F_{SF}^{sim} / d_f$  across the investigated  $\mu_s' d_f$  range. These data exhibit a distinct U-shaped profile characterized by two phases: (1) for small  $\mu_s' d_f$  values ( $\mu_s' d_f < 0.5$ ),  $F_{SF}^{sim} / d_f$  decreases in response to increases in  $\mu_s' d_f$ , and (2) for larger  $\mu_s' d_f$  values ( $\mu_s' d_f > 0.5$ ),  $F_{SF}^{sim} / d_f$  increases in response to increases in  $\mu_s' d_f$ . This bi-phasic behavior is consistent with previous observations of the influence of scattering on fluorescence collected at or near the source [20, 21]; the underlying mechanisms of these phases and their respective dependence on scattering parameters are described in detail in Section 4.

##### 3.1.2. Case II: $\mu_s'(\lambda_x) \geq \mu_s'(\lambda_m)$

The data investigated in Figure 1 are for the case  $\mu_s'(\lambda_x) = \mu_s'(\lambda_m)$ ; however, in tissue,  $\mu_s'(\lambda)$  is understood to follow a wavelength-dependent expression (e.g. Mie or Rayleigh approximations) such that  $\mu_s'(\lambda_x) > \mu_s'(\lambda_m)$ . MC simulations were used to investigate  $F_{SF}^{sim}$  for the case of independent variation of  $\mu_s'(\lambda_x)$  (range:  $[0.1 - 8.0] \text{ mm}$ ) and  $\mu_s'(\lambda_m)$  (specified as  $\mu_s'(\lambda_m) = [0.25, 0.5, 0.75, 1.0] \times \mu_s'(\lambda_x)$ ). Figures 2 A and B show linear and log representations of the full  $F_{SF}^{sim} / d_f$  data set plotted vs.  $\mu_s'(\lambda_x) d_f$ . Here, stratification of  $F_{SF}^{sim} / d_f$  measurements at  $\mu_s'(\lambda_x) d_f$  values are attributable to the influence of  $\mu_s'(\lambda_m)$  on the collected intensity. These data show clear deviation of  $F_{SF}^{sim} / d_f$  from the smooth curve displayed in Figures 1 E and F due to the independent influence of both  $\mu_s'(\lambda_x)$  and  $\mu_s'(\lambda_m)$  on SFFL intensity.

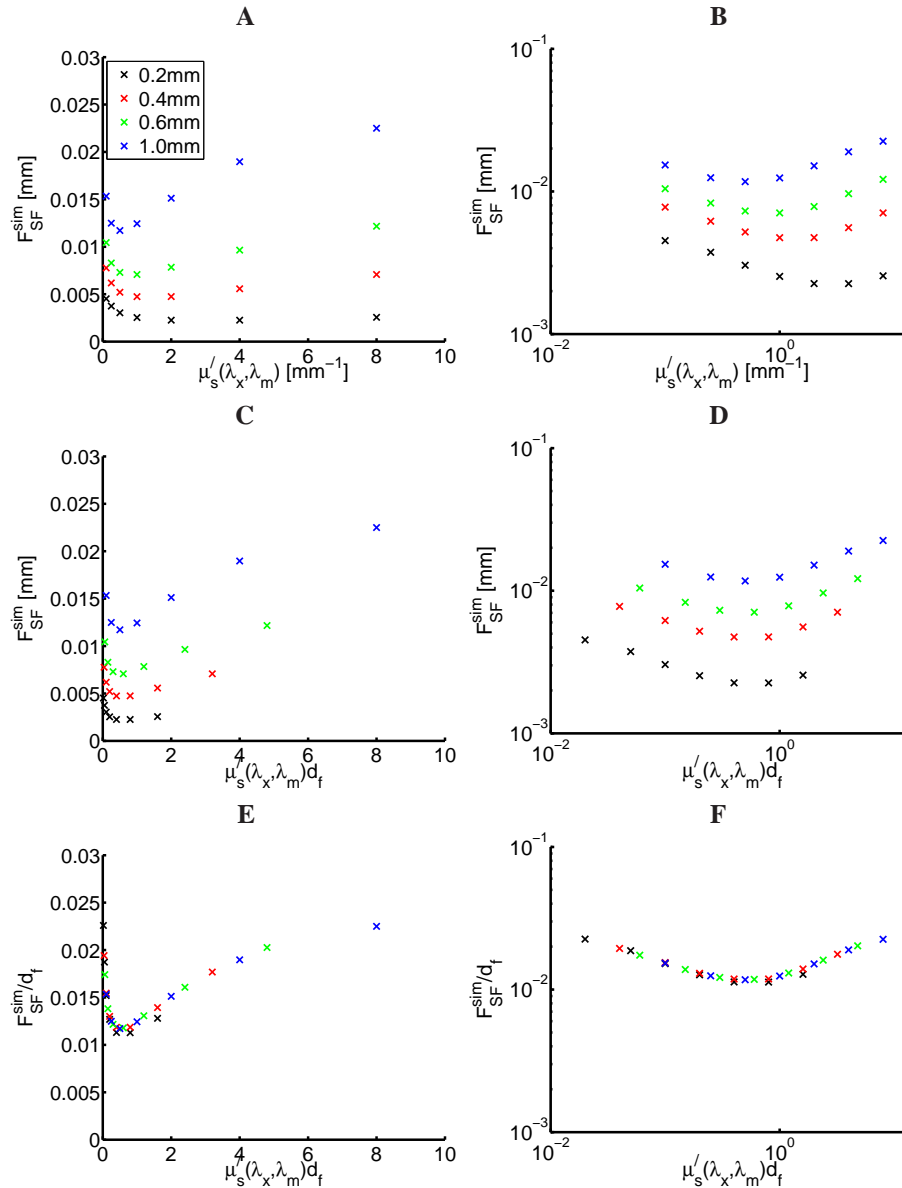


Fig. 1. Effect of reduced scattering coefficient (equivalent at  $\lambda_x, \lambda_m$ ) on single fiber fluorescence intensity. Linear and log scales of the data are presented in the following panel pairings: A and B show collected  $F_{SF}^{sim}$  vs.  $\mu'_s$ . C and D shift the x-axis to dimensionless reduced scattering  $\mu'_s d_f$ . E and F shift the y-axis to a dimensionless form of fluorescence, as  $F_{SF}^{MC} ratio/d_f$ .

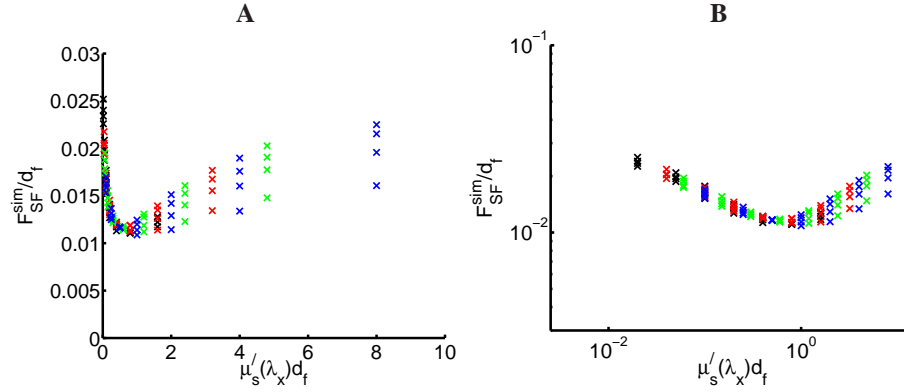


Fig. 2. Effect of independent variation of  $\mu'_s(\lambda_x)$  and  $\mu'_s(\lambda_m)$  on dimensionless single fiber fluorescence intensity,  $F_{SF}^{sim}/d_f$  plotted vs  $\mu'_s(\lambda_x)d_f$ ; vertical stratification is due to influence of  $\mu'_s(\lambda_m)$  variation. Linear and log plots given on A and B, respectively.

### 3.2. Influence of scattering phase function on $F_{SF}^{sim}$

In tissue the exact form and wavelength-dependence of the PF is not well characterized. This study utilized a subset of MC simulations to investigate in detail the influence of PF on  $F_{SF}^{sim}$ , as described in Section 2.2. The  $F_{SF}^{sim}$  showed minimal influence from variation among different phase functions, with  $< 3\%$  variation between  $F_{SF}^{sim}/d_f$  values returned from the 19 simulated PFs at each of the dimensionless reduced scattering values (data not shown). For simulations specifying different PFs at  $\lambda_x$  and  $\lambda_m$ , the simulated  $F_{SF}^{sim}$  values showed no observable difference if the PF were interchanged between the wavelengths. These results demonstrate that SFFL is insensitive to the form of the PF for all investigated scattering properties and fiber diameters.

### 3.3. Influence of fiber NA on $F_{SF}^{sim}$

This study utilized a subset of MC simulations to investigate in the influence of fiber NA on  $F_{SF}^{sim}$ , as described in Section 2.2. Simulated data showed that the effect of fiber NA on  $F_{SF}^{sim}$  is well approximated by an  $NA^2$  proportionality, with  $< 5\%$  mean residual error between estimates of  $F_{SF}$  measured by fibers of  $NA = [0.22]$  and  $NA = [0.1, 0.4]$  in the investigated scattering range (data not shown), with increasing deviations associated with decreasing dimensionless reduced scattering values.

### 3.4. Investigation and modeling of factors underlying $F_{SF}^{sim}$ dependence on scattering properties

MC simulations were used to investigate the dependence of optical sampling depth, excitation fluence, and emission escape probability within the sampled volume on  $\mu'_s(\lambda_x)$  and  $\mu'_s(\lambda_m)$  within the sampled medium; these quantities were calculated as described in Section 2.1. Figure 3A shows a dimensionless description of effective optical sampling depth, given here as  $\langle Z^{MC} \rangle / d_f$ , plotted vs.  $\mu'_{s,avg} d_f$ , with  $\mu'_{s,avg}$  calculated as the average of  $\mu'_s(\lambda_x)$  and  $\mu'_s(\lambda_m)$  for each measurement. These  $\langle Z^{MC} \rangle / d_f$  data exhibit a power law that shows a decreasing relationship with increasing  $\mu'_{s,avg} d_f$ , resulting in a 10-fold decrease over the investigated  $\mu'_{s,avg} d_f$  range. This relationship is well-characterized by Eq. (11); fitting this equation to these data yielded estimated values for  $A_2 = 0.71 \pm 0.01$  and  $A_3 = 0.36 \pm 0.01$ , and resulted in accurate

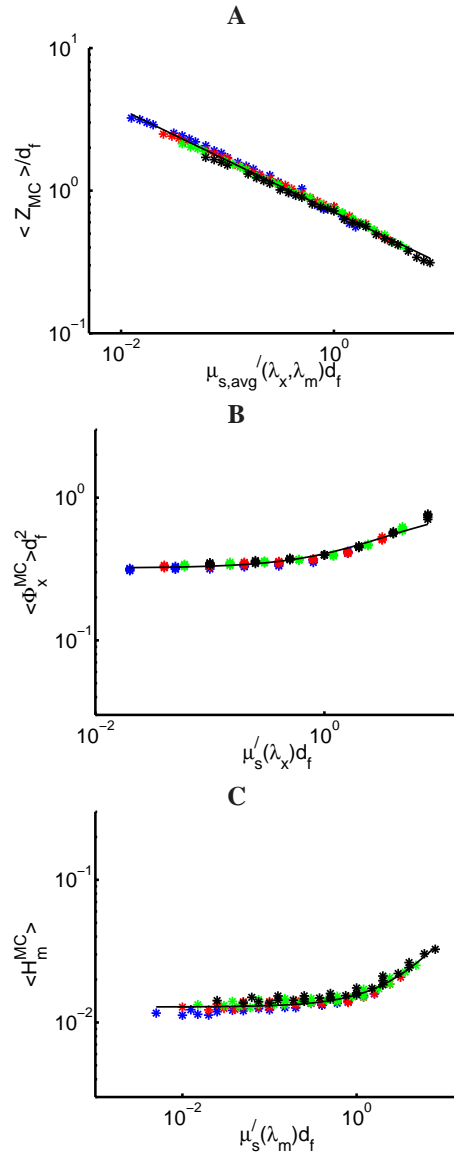


Fig. 3. A) Dimensionless sampling depth  $\langle Z^{MC} \rangle / d_f$  vs. the product of average of reduced scattering coefficients at excitation and emission wavelengths,  $\mu'_{s,avg}$  and  $d_f$ . B) Excitation fluence within the sampled volume,  $\langle \Phi_x^{MC} \rangle d_f^2$  vs. dimensionless reduced scattering at the excitation wavelength,  $\mu'_s(\lambda_x) d_f$ . C) Escape probability of emission photons,  $\langle H_m^{MC} \rangle$  vs. dimensionless reduced scattering at the emission wavelength,  $\mu'_s(\lambda_m) d_f$ . Fitted model estimates visualized by solid black lines.

estimates of  $\langle Z^{MC} \rangle / d_f$  over the full range of investigated  $\mu'_{s,avg} d_f$  values ( $r = 0.996$ ); model predictions are visualized by the solid black line on the plot.

MC simulations also returned scalar metrics representative of effective excitation fluence and effective emission escape probability within the optically sampled volume. Figure 3B displays  $\langle \Phi_x^{MC} \rangle d_f^2$  vs.  $\mu'_s(\lambda_x)$ ; these data show that  $\langle \Phi_x^{MC} \rangle$  nonlinearly depends on  $\mu'_s(\lambda_x) d_f$ , with an observed 2.5-fold increase across the investigated range. The form of the observed relationship is empirically described by Eq. (12); fitting the data to this model yielded estimated parameters of  $B_1 = 0.88 \pm 0.01$  and  $B_2 = 0.27 \pm 0.03$  and resulted in an accurate description of the simulated data ( $r = 0.977$ ); fit quality is visualized by the model estimated black line. Figure 3C displays  $\langle H_m^{MC} \rangle$  vs.  $\mu'_s(\lambda_m) d_f$ ; these data show a nonlinear dependence on  $\mu'_s(\lambda_m) d_f$ , with a 2.9-fold increase in the likelihood of collection associated with increasing  $\mu'_s(\lambda_m) d_f$ . This relationship is described by Eq. (13); the model fit to these data provides estimated parameter values of  $C_1 = 0.12 \pm 0.07$ ,  $C_2 = 0.10 \pm 0.04$ , and  $C_3 = 2.22 \pm 0.61$  and returns accurate estimates of  $\langle H_m^{MC} \rangle$  ( $r = 0.967$ ) over the investigated range of  $\mu'_s(\lambda_m)$ . These results indicate that the Eqs. (12) and (13) describe both the magnitude and dynamic trends of the respective dependencies of  $\langle \Phi_x^{MC} \rangle$  vs.  $\mu'_s(\lambda_x) d_f$  and  $\langle H_m^{MC} \rangle$  vs.  $\mu'_s(\lambda_m) d_f$ .

### 3.5. Semi-empirical model of $F_{SF}^{sim}$

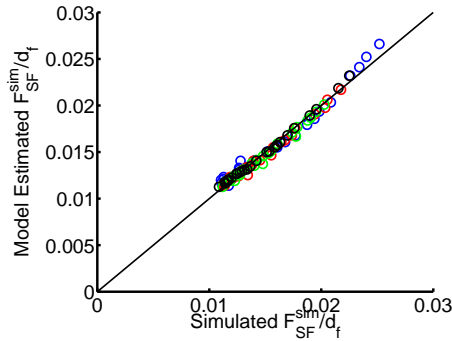


Fig. 4. Dimensionless single fiber fluorescence intensity estimated by fitted model vs. MC simulated values. Data include variations of  $\mu'_s(\lambda_x)$  and  $\mu'_s(\lambda_m)$ . Line of unity included for comparative purposes.

Figure 4 shows  $F_{SF}^{sim} / d_f$  simulated by the MC model vs. estimated by the fit of Eq. (14). Here the estimated parameter values of  $\zeta_1 = 0.0935 \pm 0.003$ ,  $\zeta_2 = 0.31 \pm 0.01$ , and  $\zeta_3 = 1.61 \pm 0.05$  resulted in the minimum weighted residual error between simulated and model-estimated  $F_{SF}^{sim}$  values. The model estimates were strongly correlated with simulated outputs, with the quality of the fit given by the Pearson correlation coefficient of  $r = 0.991$  and displayed by the proximity of the data points to the plotted line of unity. The mean absolute residual between simulated and model estimated values is  $< 3\%$  and all data points have a mean residual error that is  $< 10\%$  of the simulated value. Figures 5A and B show simulated and model estimated  $F_{SF}^{sim} / d_f$  vs.  $\mu'_s(\lambda_x) d_f$ ; this plot visualizes the capability of the model to describe the influence of both  $\mu'_s(\lambda_x)$  and  $\mu'_s(\lambda_m)$  on the collected fluorescence intensity. These results indicate that Eq. (14) provides an accurate description of the SFFL intensity over a wide range of  $\mu'_s(\lambda_x)$ ,  $\mu'_s(\lambda_m)$ , and  $d_f$ , and is valid for all investigated forms of the PF.

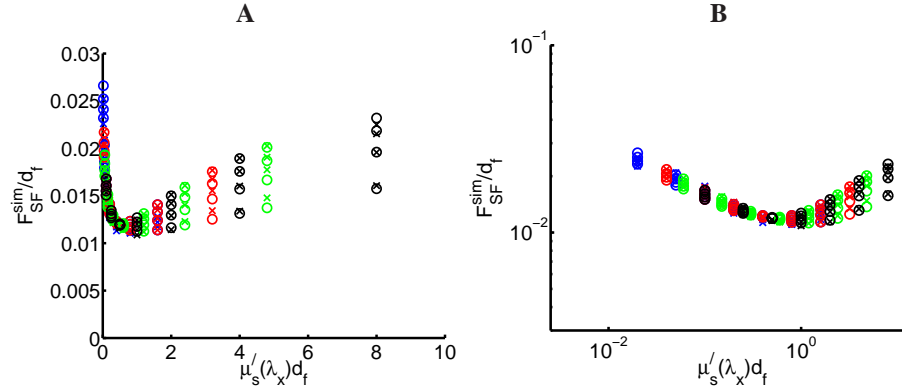


Fig. 5. Dimensionless single fiber fluorescence intensity estimated by fitted model ( $\times$  marks) and returned by MC simulations ( $\circ$  marks). Data include independent variation of  $\mu'_s(\lambda_x)$  and  $\mu'_s(\lambda_m)$ , and are plotted vs.  $\mu'_s(\lambda_x)d_f$ . Linear and log plots given on A and B, respectively.

#### 4. Discussion

This study utilizes a Monte Carlo model to characterize the relationship between the fluorescence intensity collected by a single fiber ( $F_{SF}$ ) and the scattering properties within an optically sampled turbid medium. Simulated data were used to identify a relationship between dimensionless fluorescence intensity,  $F_{SF}^{sim}/d_f$ , and dimensionless reduced scattering. We found that the collected fluorescence does not scale exclusively with dimensionless reduced scattering at the excitation wavelength, nor with dimensionless reduced scattering at the emission wavelength; rather it shows a more-complicated dependence on the reduced scattering coefficients at both wavelengths. These data were used to develop a semi-empirical model that expresses  $F_{SF}^{sim}/d_f$  as the product of an effective sampling volume, and the effective excitation fluence and the effective escape probability within the effective sampling volume. The influence of scattering properties on each of these components was identified and mathematically described using simulation outputs. The semi-empirical model of  $F_{SF}^{sim}/d_f$  accurately describes simulated fluorescence intensities over a wide range of biologically relevant scattering properties.

##### 4.1. Influence of scattering properties on $F_{SF}^{sim}$

The fluorescence model, given in Eq. (14), utilizes empirical functions to represent the individual components of the SFFL measurement, including  $\langle Z^{MC} \rangle/d_f$ ,  $\langle \Phi_x^{MC} \rangle$ , and  $\langle H_m^{MC} \rangle$ . This approach provides insight into the mechanisms underlying the bi-phasic relationship observed between  $F_{SF}^{sim}/d_f$  and the dimensionless reduced scattering coefficient, as visualized in Figure 1F. For  $\mu'_s d_f < 0.5$ , denoted as phase (1), increases in  $\mu'_s$  at either  $\lambda_x$  and  $\lambda_m$  result in a decrease in  $F_{SF}^{sim}/d_f$ . In this scattering region, the average depth of origin for collected fluorescence (and in turn the sampling depth) follows a similar trend, while the effective excitation fluence and effective emission probability are relatively insensitive to changes in this dimensionless scattering region; these trends are visualized in Figure 3. Figure 6A shows  $F_{SF}^{sim}/d_f$  data in phase (1) following a smooth and continuous dependence on  $\mu'_{s,avg} d_f$ ; this scattering dependence is shared by  $\langle Z^{MC} \rangle/d_f$ . These observations suggest that the left hand side of the  $F_{SF}^{sim}/d_f$  profile is dominated by volume effects. Here, collected fluorescent photons originate from relatively deep locations in the medium, and an increase in  $\mu'_{s,avg}$  represents an impediment to light transport (either for excitation or emission photons), resulting in a decreased tissue volume optically

sampled, and a reduced collected intensity. Conversely, for  $\mu'_s d_f > 0.5$ , denoted as phase (2), increases in  $\mu'_s$  at excitation or emission wavelengths result in an increase in  $F_{SF}^{sim}/d_f$ . In this scattering region,  $\langle \Phi_x^{MC} \rangle$  increases as  $\mu'_s(\lambda_x)$  increases, as shown in Figure 3B. This observation is attributable to the fluence 'build-up' within the turbid medium near the fiber-tip for increasing scattering [30]. Also in this scattering region,  $\langle H_m^{MC} \rangle$  increases in response to an increase in  $\mu'_s(\lambda_m)$ , as shown in Figure 3C. This phenomenon can be understood as follows. Scattering at the emission wavelength has two counteracting effects on fluorescence collection. First, fluorescent photons traveling towards the detecting fiber may be scattered away from the fibertip, decreasing the SFFL signal. This attenuating effect will be more pronounced for fluorescent photons that are emitted from relatively deep locations within the sample, while for photons originating close to the fibertip the attenuation due to scattering is expected to be small due to the small path traveled to the fibertip. Second, fluorescent photons traveling away from the detecting fiber may be backscattered towards the fibertip, increasing the SFFL signal. The balance of these counteracting effects will be depth dependent; photons originating from large depths inside the medium are expected to suffer more from attenuation due to scattering than benefit from fluorescence backscattering, while the opposite is true for photons originating close to the fibertip. Since for high scattering coefficients the effective sampling depth is relatively small, the net effect is that the benefit from fluorescence backscattering outweighs the attenuation of fluorescence due to scattering, resulting in an increase in effective escape probability with increasing scattering coefficient.  $F_{SF}^{sim}/d_f$  data in phase (2) were observed to smoothly follow a dimensionless reduced scattering parameter dependent on the harmonic average of  $\mu'_s(\lambda_x)$  and  $\mu'_s(\lambda_m)$ ; this relationship was gained from inspection of the dependence of  $\langle \Phi_x^{MC} \rangle$  and  $\langle H_m^{MC} \rangle$  on the reduced scattering coefficient. Specifically, the harmonic average reduced scattering coefficient is given as

$$\mu'_{s,h-avg} = \frac{1 + \zeta_3}{\frac{1}{\mu'_s} + \frac{\zeta_3}{\mu'_s}} \quad (16)$$

These observations suggest that the right hand side of the  $F_{SF}^{sim}/d_f$  profile (phase (2)) is dominated by a combination of excitation fluence build-up and increased fluorescence escape probability close to the fibertip for increasing reduced scattering coefficients at excitation and emission wavelengths, respectively. These observations are consistent with mechanisms that were previously proposed, but not explicitly investigated, in studies of localized [21] or single fiber measurements [20] of fluorescence.

#### 4.2. Application of semi-empirical model of $F_{SF}^{sim}$ to extract intrinsic fluorescence in turbid media

The semi-empirical model developed in this study provides a method to return scattering-independent  $F_{SF}$  quantities provided that  $\mu'_s(\lambda_x)$  and  $\mu'_s(\lambda_m)$  are determined, *e.g.* from a white-light reflectance measurement. This approach is in contrast to other techniques that utilize raw reflectance to correct raw fluorescence for the influence of scattering properties. Such an approach is not appropriate for single fiber measurements, because reflectance intensities collected by single fibers ( $R_{SF}$ ) are not only sensitive to  $\mu'_s$ , but (in contrast to SFFL) are also heavily influenced by the PF [24, 31, 32]. Due to this difference in PF dependence of  $F_{SF}$  and  $R_{SF}$ , the ratio of these two quantities will also be PF dependent. The magnitude of this dependence can best be appreciated by considering  $R_{SF}$  measurements of two (hypothetical) turbid media with  $\mu'_s$  values of 0.5 and 2.0  $\text{mm}^{-1}$ , both with the same intrinsic fluorescence, and measured by a fiber with  $d_f = 1.0$  mm. If the PF within the two media were varied from  $\gamma = 1.9$  to  $\gamma = 1.4$  (a change that would increase the likelihood of large-angle scattering events), the resulting  $R_{SF}$  would increase by a factor of 2.3 for  $\mu'_s = 0.5 \text{ mm}^{-1}$  and a factor of 1.4 for  $\mu'_s = 2.0$

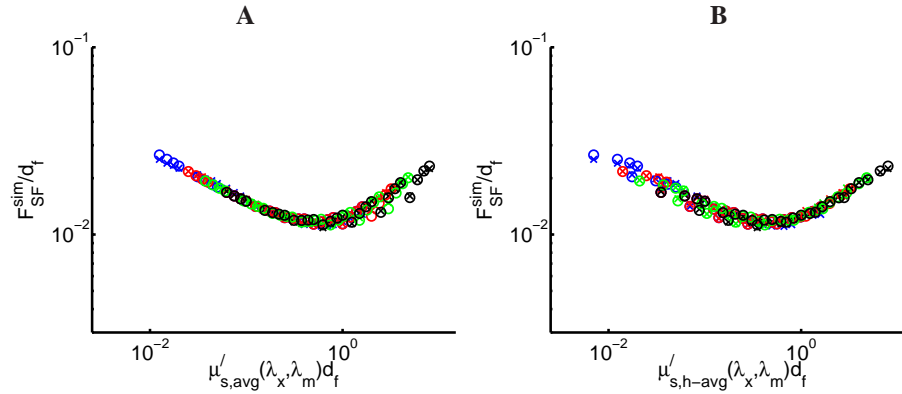


Fig. 6. Dimensionless single fiber fluorescence intensity plotted vs. dimensionless reduced scattering calculated as A) mean of  $\mu'_s(\lambda_x)$  and  $\mu'_s(\lambda_m)$  and B) harmonic average expression including  $\mu'_s(\lambda_x)$  and  $\mu'_s(\lambda_m)$ , given in Eqn 16. Smooth dependence of fluorescence intensity vs. these respective scattering parameters suggests region  $\mu'_s d_f < 0.5$  is dominated by volume effects, region  $\mu'_s d_f > 0.5$  is dominated by excitation fluence and emission probability within sampled volume.

$\text{mm}^{-1}$  [24, 25]. For a smaller fiber of  $d_f = 0.2$  mm, the effects are amplified to factors of 3.1 and 1.5 for each respective case. Importantly, the variation in PF would have a negligible effect on the raw  $F_{SF}$ ; such a difference in sensitivity to PF is attributable to the isotropic release of emission photons during propagation of fluorescent light. In contrast to  $R_{SF}$ , which relies on the likelihood of forward directed incident light to undergo a large-angle scattering event (defined by the PF), the isotropic release of a fluorescent photon greatly reduces the sensitivity of  $F_{SF}$  to PF. Therefore, for single fiber measurements (and likely other geometries which collect light close to the source fiber), a fluorescence correction algorithm that utilized a ratio of  $F_{SF}$  and  $R_{SF}$  could result in inaccurate estimation of intrinsic fluorescence by a factor of  $> 3$  for small dimensionless scattering values.

The PF-specific analysis presented in this study indicates that quantitative analysis of SFFL requires determination of  $\mu'_s(\lambda_x)$  and  $\mu'_s(\lambda_m)$  independent of PF. This could be achieved using a multi-diameter SFR measurement, as described recently by our group [25,26]. The MDSFR approach utilizes the  $\gamma$ -specific  $R_{SF}$  vs.  $\mu'_s d_f$  relationship for measurements using multiple fibers at each investigated wavelength. By specification of a background scattering model within the sampled tissue (*e.g.* Mie and or Rayleigh scattering) it is possible to determine  $\mu'_s$  and  $\gamma$  across the a range of wavelengths. Moreover, this calculation can be made in the presence of absorption from tissue chromophores, requiring only specification of the basis set of absorbing constituents and their respective specific absorption coefficients. This multi-fiber approach can be executed using as few as two optical fibers with different diameters [26]; moreover, such a device can easily be developed to sample both  $R_{SF}$  and  $F_{SF}$ . The combined multi-diameter SFR and SFFL would return paired local measurements of fluorescence and tissue optical properties within the same (shallow) sampling volume. Such a technique has the potential to provide clinically useful information for tissue diagnostics and monitoring of administered therapies. The localized measurement volume would allow quantitative characterization of heterogeneities in the spatial distribution of an administered fluorescent compound; this may be advantageous compared with a volume-averaged metric gained from diffuse optical measurements. Moreover, the measurement volume can be selected at a specific area of interest (*e.g.* in the center of an identified malignant area, or on the border between suspicious and normal tissue). This

multi-fiber approach faces challenges that must be properly assessed, including proper identification of background scattering models for determination of  $\mu'_s(\lambda)$ , the influence of  $\mu_a$  on  $F_{SF}$ , and the influence of heterogeneities on both  $R_{SF}$  and  $F_{SF}$ ; ongoing studies are investigating these issues.

#### 4.3. Limitations and future work

In order to appropriately utilize the semi-empirical model of SFFL presented in this study, it is important to consider the assumptions and approximations utilized in its development. The mathematical modeling approach utilized in this study represents the collected fluorescence intensity in terms of the product of three factors contributing to fluorescence that were extracted from Monte Carlo models outputs; these relationships are presented in the transition from Equation 6 to 10. A critical assumption of this modeling approach is that the effective scalar values for these components are representative of the more complicated 2-D maps of these properties. The empirical models of each of the components expresses a high quality of fit, providing evidence that this assumption is reasonable. Another important point of this study is the specific investigation of a single optical fiber in contact with a turbid medium; the exact form of the expressions governing light transport have been defined for this geometry. While the approach to modeling SFFL utilized here is extensible to modifications in measurement geometry, it is important to note that changes to the geometry will result in changes to the excitation and emission light distributions, and will require assessment of the appropriateness and accuracy of the specified model structures. Such modifications include interstitial placement of the fiber optic in the sampled medium, or placement of the fiber optic into a probe face surrounded by epoxy, metal, or other optical fibers; ongoing work is investigating these influences. Another important consideration is that this study characterized the scattering dependence of  $F_{SF}$ , and did not consider background absorption effects. Absorption within the sampled medium, at both excitation and emission wavelengths, is expected to have a substantial influence on the raw fluorescence intensity collected and the volume probed during measurement. Further complicating matters, the magnitude of the absorption attenuation is expected to be heavily influenced by the paired scattering properties at excitation and emission wavelengths. An ongoing study will characterize the influence of absorption on the individual components of the SFFL model. Additionally, the MC model utilized in this study was validated by comparison with model returned outputs reported in the literature; future work will conduct experimental validation in optical phantoms.

## 5. Conclusions

In summary, the current study utilized MC simulations to investigate the influence of scattering properties on fluorescence intensity collected by a single fiber probe. Simulated data were used to identify an underlying dimensionless relationship between fluorescence intensity and dimensionless reduced scattering. Results indicate that the mathematical model of  $F_{SF}$  is valid over a wide range of reduced scattering coefficients, in the range  $\mu'_s(\lambda_x) \in [0.1 - 8] \text{ mm}^{-1}$  and  $\mu'_s(\lambda_m) \in [0.25 - 1] \times \mu'_s(\lambda_x)$ , and scattering phase functions ( $P(\theta)$ ), with both Henyey-Greenstein and Modified Henyey-Greenstein forms with anisotropy in the range 0.5 – 0.95 and  $\gamma \in [1.4 - 1.9]$ , and a wide range of fiber diameters ( $d_f \in [0.2 - 1.0] \text{ mm}$ ). The model accurately estimates  $F_{SF}$  given  $\mu'_s(\lambda_x)$  and  $\mu'_s(\lambda_m)$ , and is insensitive to the anisotropy and higher order moments of the PF. Results indicate that correction for the influence of scattering on  $F_{SF}$  requires estimation of scattering optical properties from a paired measurement of white-light reflectance.